

Experimental implementation of a discrete-time quantum walk on biological networks

Viacheslav Dubovitskii^{1,*}, Filippo Utro², Aritra Bose², Laxmi Parida², Sabrina Maniscalco¹, and Sergey N. Filippov¹

¹Algorithmiq Ltd, Kanavakatu 3 C, FI-00160 Helsinki, Finland

²IBM Quantum, Yorktown Heights, NY, USA

*Corresponding author: viacheslav.dubovitskii@algorithmiq.fi

ABSTRACT

Quantum walks provide a versatile framework for probing the structural and dynamical properties of complex systems ranging from biological networks to synthetic materials. However, their realization on current noisy pre-fault-tolerant quantum computers is fundamentally limited by decoherence. Conventional dense encodings of graph structures require prohibitively deep circuits, making them incompatible with existing hardware. Here we introduce an algorithm that leverages symmetry-sector encoding and trades circuit depth for qubits, while integrating symmetry-respecting postselection as an effective noise-mitigation strategy. This combination enables us to execute practical quantum-walk circuits for biological networks on actual quantum hardware. We benchmark the proposed methodology against known state-of-the-art circuit architectures, highlighting significant reduction of circuit depth in our approach at the cost of moderate qubit overhead. Utilizing 40 qubits, we implement quantum walks on complex graphs containing up to 17 nodes and 20 edges—the largest experiment on superconducting hardware to date, with the Hellinger fidelity exceeding 87% throughout 7 steps. We present a case study that illustrates how experimentally obtained quantum-walk dynamics on a protein-protein-interaction network can be applied to prioritizing disease-associated genes. We discuss the framework scalability in the pre-fault-tolerant era and its potential for studying larger biological networks.

Introduction

Network medicine offers a systematic approach to understanding complex disease mechanisms by examining interactions within biological networks, a cornerstone of precision medicine. In this context, quantum walks (QWs), which leverage quantum principles such as superposition and interference, have emerged as a promising method for modeling information spreading on graphs. Their appeal lies in the ability to capture richer propagation dynamics and explore network topology more deeply than classical approaches^{1–3}. Recent studies have demonstrated the potential of QWs in addressing key challenges in network medicine, including link prediction, disease target identification, network propagation, and node classification^{4–8}.

Among the different QW formulations³, discrete-time quantum walks (DTQWs) have seen significant theoretical progress toward implementation on present-day digital quantum processors. However, despite advances in circuit design, their practical implementation on current quantum computers has been constrained by current hardware limitations such as gate and measurement errors, leakage noise, and restricted qubit connectivity^{9–14}.

Earlier work on DTQW implementation, conducted during periods of qubit scarcity, prioritized minimizing the required number of physical qubits^{15–18}. Most circuit-based DTQW implementations used $\lceil \log_2 N \rceil$ qubits (dense encoding for N walker positions) plus a coin qubit, realizing increment-decrement update rules^{17–20}. Ancilla-free and coinless constructions pushed this reduction even further. While these approaches enabled early experimental demonstrations, they often did so at the cost of substantially increased multi-controlled gate complexity leading to deeper circuits that typically degrade overall fidelity²⁰. Consequently, few implementations targeting multiple walk steps consistently reported improved performance when multi-controlled gates were reduced or avoided altogether^{20,21}, yet they remained feasible only on small graphs.

To mitigate resource overhead, several gate-level optimizations have been proposed. In particular, diagonalizing the shift operator via a quantum-Fourier-transform-based decomposition reduces the circuit to linear depth with quadratic gate complexity^{17,19}. Some additional mappings reuse identical sub-circuits (e.g., via parity encoding) and eliminate unnecessary operations, halving the gate count compared to the naïve encodings²². Techniques that exploit predictable least significant bit behavior and intermediate qudit levels avoid ancillas and keep circuits comparatively compact^{23,24}.

As qubit quality improved, larger DTQW experiments became possible^{19,21,25}. However, hardware-informed classical simulations indicated that executing larger DTQWs (e.g., on a 16-node graph over 16 steps) still required significantly lower noise levels to maintain acceptable fidelity^{21,25}. For instance, an experiment with 4-qubit circuit (8-vertex cycle graph) achieved fidelity 0.8 for up to 13 steps, whereas an experiment with 3-qubit circuit (4-vertex cycle graph) reached the fidelity nearly 0.9

for up to 19 steps. The latter experiment benefits from the specific structure of the 4-vertex cycle graph that allowed the circuit depth be almost independent of the number of time steps¹⁹, a property that does not generalize to other graphs.

From a resource perspective, even with access to high nominal gate fidelities, dense encoding remains impractical, as decoherence limits reachable Hilbert space by degrading superposition and entanglement. More advanced encoding schemes address this by applying position-dependent coin operators in parallel by introducing ancillary position and coin wires, trading circuit depth for ancilla count. An adjustable-depth approach groups the position-dependent coins into packs of size $M = 2^m$, with m representing the depth, so that only M coins are applied per stage. As m increases, the design transitions from sequential to fully parallel and reduces multi-Toffoli and total gate count²⁶. These schemes illustrate a deliberate transition toward using more qubits to enable deeper parallelism and control, at the expense of ancilla overhead.

The previously discussed DTQW implementations employ approaches designed for regular graphs (e.g., lines, cycles, lattices) and were validated primarily on these topologies, which limits generalization to irregular or heterogeneous networks such as those arising in biological settings^{19–21}. In response, in order to extend DTQW circuits to irregular and complex networks Refs.^{27–30} deal with an encoding in which position and coin registers explicitly represent node (i) and outgoing-edge labels ($i \rightarrow j$). While structurally transparent, the design of Ref.²⁸ enables a simple SWAP-based shift; however, it requires coin operations conditioned on node-specific bit patterns, typically through ancilla assisted checks. As graph structure becomes more heterogeneous, this results in rapidly increasing circuit depth and makes the approach difficult to scale beyond highly regular topologies. Ref.²⁹ allocates $\lceil \log_2 N \rceil$ qubits to node positions and $\lceil \log_2 |E| \rceil$ qubits to $|E|$ edge labels, whereas recent Ref.³⁰ exploits $2\lceil \log_2 N \rceil$ qubits in a dual-register encoding. Position-dependent coins of varying size are implemented via generalized diffusion operators on the edge register, enabling rotations over internal degrees of freedom without redesigning the coin at each node. This avoids vertex specific conditional logic and yields more predictable circuit depth on irregular networks. Functionality of these approaches is validated on an 8-node complex network via classical simulation²⁹ and experiment³⁰, though their dependence on deep multi-controlled gate structures limits its robustness under realistic noise models.

Across these developments, advanced error-suppression strategies are rarely employed, leaving fidelity to depend on circuit shallowness rather than algorithmic techniques. In this context, Cai’s review highlights a simple yet effective mitigation approach: identify violations of the symmetries of the ideal quantum state and remove them via postselection¹¹. However, making symmetry checks feasible on hardware requires an encoding that exposes measurable symmetries and avoids excessive multi-controlled gates that amplify noise.

Motivated by this need, we introduce an alternative encoding of DTQW states that trades circuit depth for qubit count (twice the number of edges, $2|E|$), a feasible approach on currently available large-scale quantum computers. By encoding information in a specific symmetry sector of the Hilbert space, we significantly reduce circuit depth, while symmetry-respecting postselection enables efficient noise mitigation. It is the combination of reduced circuit depth and the postselection in the proposed algorithm that makes the DTQW less susceptible to noise, leading to the largest DTQW implementation on complex graphs to date (40 qubits and a depth exceeding 200 entangling layers), in contrast to the regular or symmetric structures explored previously^{19,23,31}. Our design handles graphs with the nonuniform degree distributions typical of biological networks. We implement the DTQW experimentally on IBM’s quantum hardware with heavy-hex connectivity and show how the resulting propagation dynamics enables the disease-target identification. While universal scalability remains a long-term objective, our design introduces a distinct paradigm by prioritizing hardware-efficient mapping, providing a practical path toward maximizing the utility of current quantum computers.

The paper is organized as follows. The Results section presents our framework for implementing DTQWs on arbitrary complex networks using current quantum computers, including the proposed encoding and postselection strategies, and demonstrates its feasibility through practical hardware experiments on three biologically relevant graphs. We then compare our encoding approach with other baselines in terms of the circuit size, depth, and accuracy, yielding insights into circuit scalability and optimization. A case study illustrates how experimentally obtained DTQW dynamics can be applied to prioritizing disease genes. The Discussion section contextualizes these findings and outlines future directions, while Methods detail the DTQW formulation and the procedures used for performance evaluation and quantum-walk-based node prioritization.

Results

Implementation framework

We present a novel framework for implementing DTQW on arbitrary complex networks. The framework is designed to be compatible with digital gate-based quantum processing units (QPUs). Consider a network with N nodes $V = \{1, 2, \dots, N\}$ and undirected edges $E = \{\{i, j\} \mid i \text{ and } j \text{ are adjacent}\}$. The DTQW Hilbert space is spanned by the directed-edge states $|i \rightarrow j\rangle$ that represent a walker at node i which is about to hop to adjacent node j ²⁷. The Hilbert space dimension is $2|E|$ and coincides with the number of directed edges $(i, j) \in E_{\text{dir}}$. The quantum state $|\psi(t)\rangle$ of the DTQW at step t is defined in the abstract

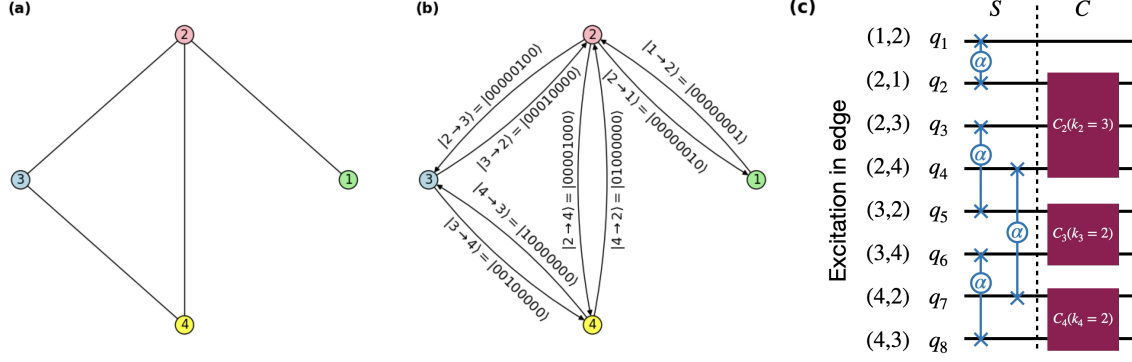


Figure 1. Implementation framework. (a) Example 4-node graph. Nodes 1, 2, 3, and 4 have degree 1, 3, 2, and 2, respectively. (b) Encoding DTQW states $|i \rightarrow j\rangle$ into qubit states. The length of qubit register is twice the number of graph edges. (c) Single-step in DTQW circuit consisting of the shift and coin operators. The shift operator S represents a collection of partial-swap gates associated with opposite directions within the same edge, whereas the coin operator C is composed of the smaller Grover coins C_i associated with the graph nodes i of degree k_i . Qubits carry information about excitations (walker) in the corresponding graph edges.

$2|E|$ -dimensional Hilbert space as

$$|\psi(t)\rangle = \sum_{(i,j) \in E_{\text{dir}}} \psi_{ij}(t) |i \rightarrow j\rangle. \quad (1)$$

The probability of finding the walker at node i is

$$P_i(t) = \sum_{j: (i,j) \in E_{\text{dir}}} |\langle i \rightarrow j | \psi(t) \rangle|^2 = \sum_{j: (i,j) \in E_{\text{dir}}} |\psi_{ij}(t)|^2. \quad (2)$$

The structure and complexity of our implementation are determined by the encoding of states $|i \rightarrow j\rangle$ into the qubit space. Specifically, we represent the DTQW state $|\psi(t)\rangle$ through computational basis states restricted to the single-excitation subspace³², $|0 \dots 001\rangle, |0 \dots 010\rangle, \dots |1 \dots 000\rangle$, i.e., the states of Hamming weight 1 also known as the bracelet states. Hence, in the target qubit space, the walker's position and direction is represented by basis states where only one qubit is in the excited state $|1\rangle$. We motivate our choice by the presence of energy loss that makes basis states with higher Hamming weight less stable in time as qubits typically tend to decay from the excited state $|1\rangle$ to the ground state $|0\rangle$. This approach requires as many qubits as double-counting of graph edges, $2|E|$, and exploits the single-excitation symmetry for robustness of noise-reduction algorithms. We illustrate the encoding approach on a small graph consisting of four edges shown in Fig. 1.

We prepare the initial state $|\psi(0)\rangle$ as a uniform superposition of the states residing on a specific node i_0 of interest (seed in a biological network),

$$|\psi(0)\rangle = \frac{1}{\sqrt{k_{i_0}}} \sum_{j: (i_0,j) \in E_{\text{dir}}} |i_0 \rightarrow j\rangle, \quad (3)$$

where k_{i_0} is the degree of node i_0 . In our encoding, the initial state is entangled and represents a W -state³³ whose preparation on a quantum computer is both straightforward and efficient.

We consider the DTQW with the evolution operator $U = (CS)^t$ for step t , where C (S) is a coin (shift) operator. The coin operator is of a Grover type, because its phases are invariant under the permutation of neighboring nodes $\{j_1, j_2, \dots, j_{k_i}\}$ ³⁴ (see details in Methods). Importantly, we introduce two innovations. First, in order to achieve an efficient decomposition of the quantum circuit into native gates on a hardware with limited connectivity (e.g., heavy-hex), we label the states $|i \rightarrow j\rangle$ resting on the same node i with the neighboring bracelet states to keep the minimal Hamming distance in the qubit gate operations within the coin operator. Second, in the considered biological networks, where nodes have degrees 1, 2, and 3, the depth of the coin-operator circuit is additionally reduced by means of the appropriate basis rotation (see Methods).

In contrast to the shift operator realized via the swap gates²⁷ that effectively flips the state $|i \rightarrow j\rangle$ to $|j \rightarrow i\rangle$, our formulation generalizes this structure by introducing a tunable parameter α , which models quantum interference between forward and backward transitions:

$$S|i \rightarrow j\rangle = \sqrt{1-\alpha}|j \rightarrow i\rangle + i\sqrt{\alpha}|i \rightarrow j\rangle. \quad (4)$$

The case $\alpha = 0$ corresponds to no transitions, whereas $\alpha = 1$ realizes a swap operation that does not increase the number of interfering terms (the operation is non-entangling in the qubit space) and introduces an imbalance between odd and even evolution steps. We therefore choose $\alpha = 1/2$ corresponding to an \sqrt{i} SWAP operation that creates maximal coherence in the subspace spanned by $|i \rightarrow j\rangle$ and $|j \rightarrow i\rangle$ and is maximally entangling in the qubit space.

To find a probability distribution (2) of the walker at step t , we compose the circuit as follows: an initial-state preparation (3), followed by alternating blocks of the shift and coin operators (a total of $2t$ blocks), and finally measurement in the computational basis. The circuit is executed multiple times to ensure statistically meaningful outcomes.

Due to a presence of noise in both quantum gates and measurements, the experimental design is intentionally built to make allowance for that: only measurement outcomes with Hamming weight equal to 1 are retained for computing the probability (2). It is the postselection of measurement bitstrings from the single-excitation subspace that serves as an effective noise filter and substantially improves fidelity. After postselection, the retained measurement outcomes are aggregated according to graph connectivity to yield the node-level probabilities (2). The resulting probabilities for progressively increased time steps t constitute the basis for downstream biological data analysis.

Hardware experiment on biological data

To evaluate the practical applicability of the DTQW circuit design described above, we applied it to three graphs derived from real-world biological data. The construction of these graphs, along with the procedures for qubit mapping circuit optimization, and QPU data processing, is described in Methods. Following the proposed framework, we built quantum circuits corresponding to 7 DTQW steps for each graph. The characteristics of the graphs and the corresponding circuits are summarized in Table 1.

Table 1. Structural properties of biological networks, corresponding quantum circuits, and performance indicators.

Biological graph					Transpiled quantum circuit									Performance	
#	Nodes		Edges		Qubits	Entangling layers across time steps							CZ gates per step	Fidelity	
	N	$ E $	Diameter	Density		1	2	3	4	5	6	7		F_H	F_{HBC}
1	11	12	6	0.22	24	36	66	96	126	157	191	223	165	≥ 0.95	≥ 0.71
2	15	18	8	0.17	36	52	86	120	154	188	231	264	286	≥ 0.9	≥ 0.46
3	17	20	8	0.15	40	45	85	125	165	205	245	287	322	≥ 0.87	≥ 0.54

Analysis of the experimentally obtained results for all three graphs is summarized in Figs. 2, 3, and 4. The discrepancy between the measured and classically simulated distributions is quantified using the Hellinger fidelity F_H and its baseline-corrected version F_{HBC} (see Table 1 and Methods). As shown in panels (c) in Figs. 2, 3, and 4, the experimental distributions without postselection are in poor agreement with the ideal distributions. This mismatch is particularly visible at the first steps of the DTQW (panels (d)), where high nonuniformity in the probability distribution is expected: the corresponding F_H values before postselection are 0.69, 0.50, and 0.47, respectively (see panels (e)). This shows that the advanced encoding alone cannot fully preserve coherence.

In contrast, the postselection substantially improves the agreement between the experimental and ideal distributions—the Hellinger fidelity of the resulting probability distributions remains above 0.95 for the 24-qubit circuit and above 0.87 for larger circuits across all DTQW steps. Notably, despite the exponential decrease in the postselection ratio with increasing t (see panels (f)), the symmetry-respecting outcomes remain sufficiently coherent within the endcoding subspace, demonstrating the effectiveness of this noise-suppression approach. The same improvement due to postselection is also visible in the baseline-corrected Hellinger fidelity, which is a more sensitive performance metric in the case the distributions are close to uniform. Overall, these observations confirm that the accuracy of the implemented DTQWs benefits from two complementary approaches: encoding of information within specific symmetry sector of the Hilbert space and applying postselection to preserve this symmetry.

Our approach enables multi-step DTQWs on complex graphs at scales that prior hardware demonstrations have typically not reached, with comparable instances often treated only in simulation^{23,26,29}. Most experimental DTQW implementations to date have relied on alternative encodings and have reported moderate fidelities (e.g., 0.72–0.9), which in practice has limited demonstrations to the 3–6 qubit range and typically 1–4 walk steps^{15,17,19,20,31}. By contrast, we implement DTQWs using 24–40 qubits on 11–17 node complex graphs while retaining high agreement with the ideal distributions (F_H equals 0.95 and 0.9, respectively). This comparison indicates that our circuit construction supports substantially larger and less regular graphs on hardware, which is particularly important for biological networks with nontrivial connectivity patterns.

A case study: Disease gene prioritization

Discovery of disease pathways typically involves identifying all disease-associated proteins, grouping these proteins into coherent pathways, and analyzing how the resulting pathways connect to the disease at molecular and clinical levels³⁵.

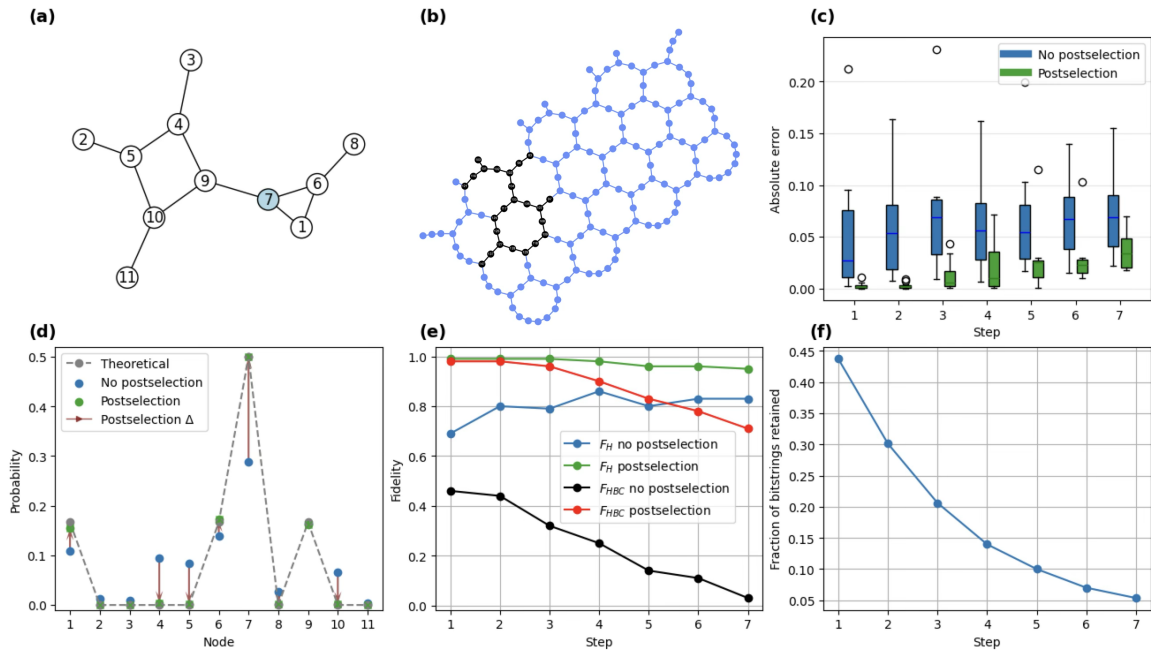


Figure 2. Quantum walk on an 11-node, 12-edge graph (24-qubit encoding). (a) Subgraph extracted from the BioPlex 3.0 PPI network. Nodes 1–11 correspond to genes PON2, VAMP5, MTOR, LYPD3, FLVCR1, HLA-C, HLA-DQA1, HLA-G, TMEM214, FAM234B, and ADPGK, respectively. Quantum walker is initialized at the highlighted node. (b) 24-qubit circuit layout for the experiment performed on `ibm_kingston` with heavy-hex connectivity. (c) Boxplot of absolute errors between experimental and simulated probabilities across nodes per step. (d) Probability distribution at Step 1. Brown vertical arrows show the change between paired probabilities introduced by postselection for each node. (e) Fidelity with and without postselection. (f) Postselection ratio across steps.

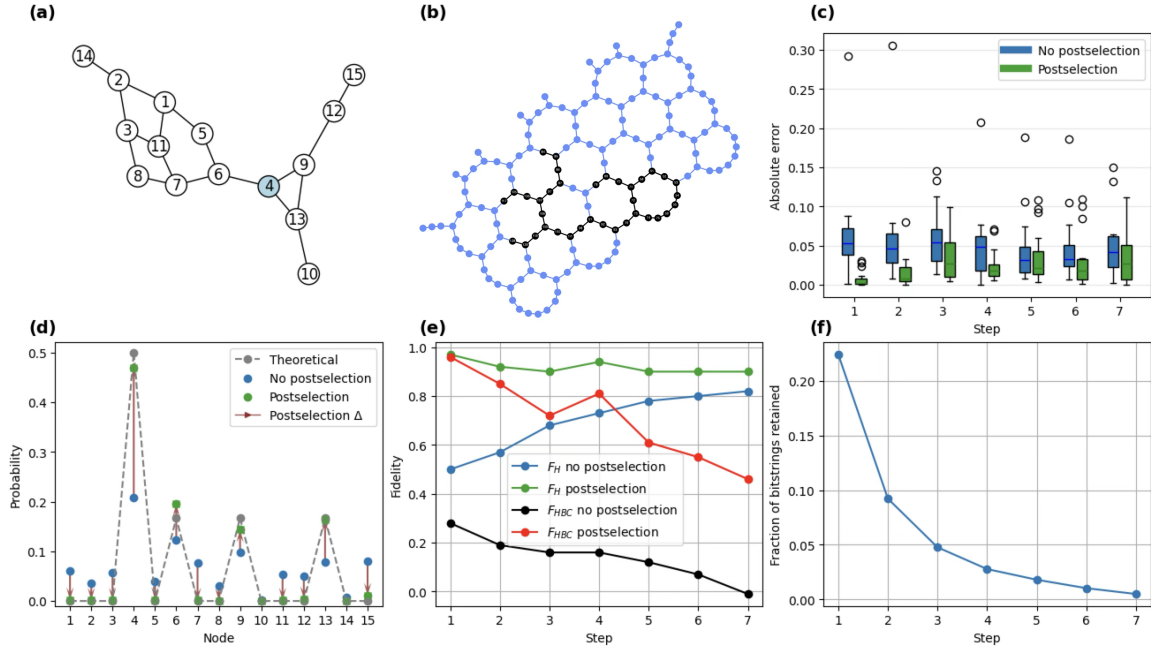


Figure 3. Quantum walk on a 15-node, 18-edge graph (36-qubit encoding). (a) Subgraph extracted from the BioPlex 3.0 protein–protein interaction network. Nodes 1–15 correspond to genes IGF2BP3, APOBEC3D, APOBEC3F, SF3B1, TRUB2, ABT1, ZFR, RBMS2, SNRPA1, SNRPB2, LIN28A, COIL, PHF5A, YTHDC1, SART3, respectively. Quantum walker is initialized at the highlighted node. (b) 36-qubit circuit layout for the experiment performed on `ibm_pittsburgh` with heavy-hex connectivity. (c) Boxplot of absolute errors between experimental and simulated probabilities across nodes per step. (d) Probability distribution at Step 1. Brown vertical arrows show the change between paired probabilities introduced by postselection for each node. (e) Fidelity with and without postselection. (f) Postselection ratio across steps.

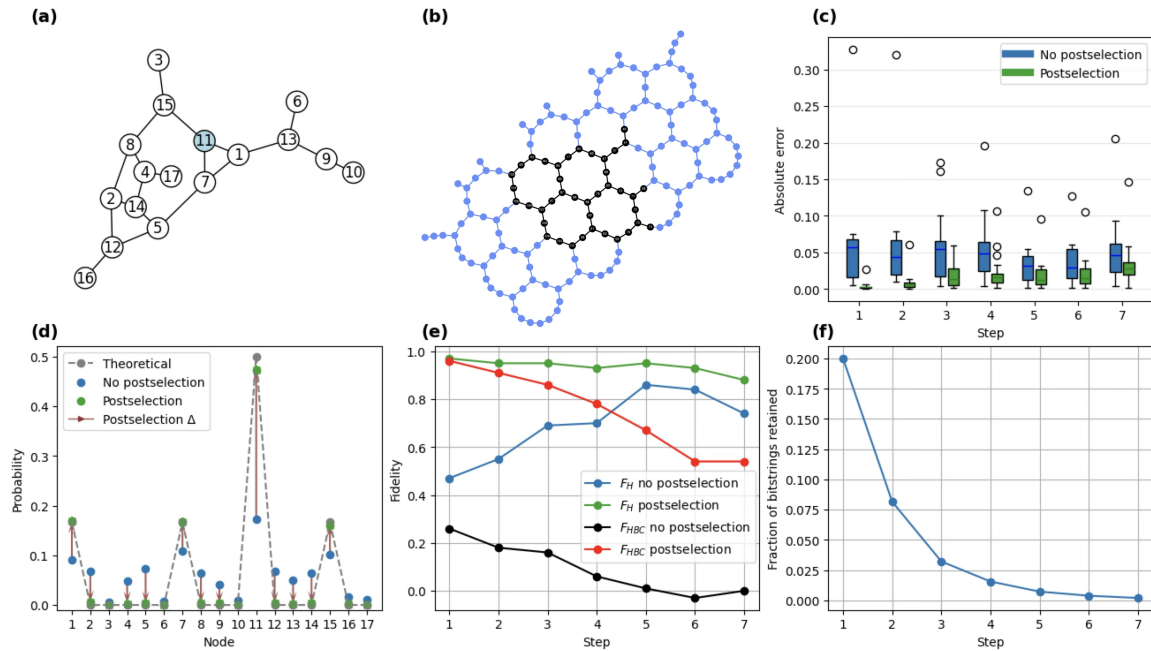


Figure 4. Quantum walk on a 17-node, 20-edge graph (40-qubit encoding). (a) Subgraph extracted from the BioPlex 3.0 PPI network. Nodes 1–17 correspond to genes AHCYL1, ATF7, AGAP3, ATF2, EEF1D, GPC4, AHCYL2, FOSL2, GPC1, HADHA, NFKBIL1, BATF3, CAMKV, FOSL1, KBTBD7, RTL6, CREB5, respectively. Quantum walker is initialized at the highlighted node. (b) 40-qubit circuit layout for the experiment performed on `ibm_kingston` with heavy-hex connectivity. (c) Boxplot of absolute errors between experimental and simulated probabilities across nodes per step. (d) Probability distribution at Step 1. Brown vertical arrows show the change between paired probabilities introduced by postselection for each node. (e) Fidelity with and without postselection. (f) Postselection ratio across steps.

Network-based methods used for disease protein discovery often operate on the PPI network: given a set of known disease proteins—referred to as seeds—the goal is to predict additional proteins, or targets, that are likely to be associated with the disease. Because many disease pathways are fragmented and weakly embedded within the global interactome, an effective prediction method must be able to operate robustly under such topological constraints³⁶. DTQWs, which model probabilistic transitions across the network while simultaneously exploring both local and global structures, are naturally suited to this task.

Here, we demonstrate how DTQW dynamics can discover asthma-related pathways by prioritizing asthma-associated nodes within the PPI graph shown in Fig. 2. In this graph, the node 7, corresponding to HLA-DQA1*, is selected as the starting point for initializing the walker, as it represents prior knowledge about the disease and is one of the most significant asthma-associated genes pertinent to the lowest P-value in genome-wide association studies (GWAS)^{37,38†}.

We expect that interference makes the walker’s probability distribution diverge from the classical one during walker’s propagation from the initial node. The nodes, where the divergence is especially visible, are associated with the structural peculiarities of the network. Since the emergence of interference patterns becomes more pronounced only after sufficient propagation depth, we ran two more experiments in addition to probability distributions obtained in 24-qubit experiments reaching 9 DTQW steps. As detailed in Methods, we compare the resulting probability distributions with those of a classical random walk to calculate the quantum interference index and assign scores to nodes on its basis, see Fig. 5. Table 2 indicates that four genes with the highest scores are indeed relevant to asthma according to literature and GWAS data.

Three highly-prioritized genes—PON2‡, HLA-C, and HLA-G§—are located near the seed node and were visited early in the walk, consistent with their proximity in the network. In contrast, gene FVCR1¶ with the fourth largest score has no direct graph connections to either the seed node or its neighbors. The prioritization of this node is attributed to amplitude interference rather than simple topological closeness, highlighting DTQW dynamics’ ability to uncover non-local yet disease-relevant genes. Importantly, FLVCR1 meets the GWAS significance threshold and has been associated with asthma across age groups³⁹.

*Major histocompatibility complex, class II, DQ alpha 1. Hereafter, we resort to a naming convention established by international workshops to categorize genetic regions.

†HLA-DQA1 lies within the HLA-DQ region, repeatedly implicated in asthma susceptibility through large-scale GWAS and fine-mapping analyses.

‡Paraoxonase 2

§Major histocompatibility complex, class I, G

¶Choline and heme transporter 1

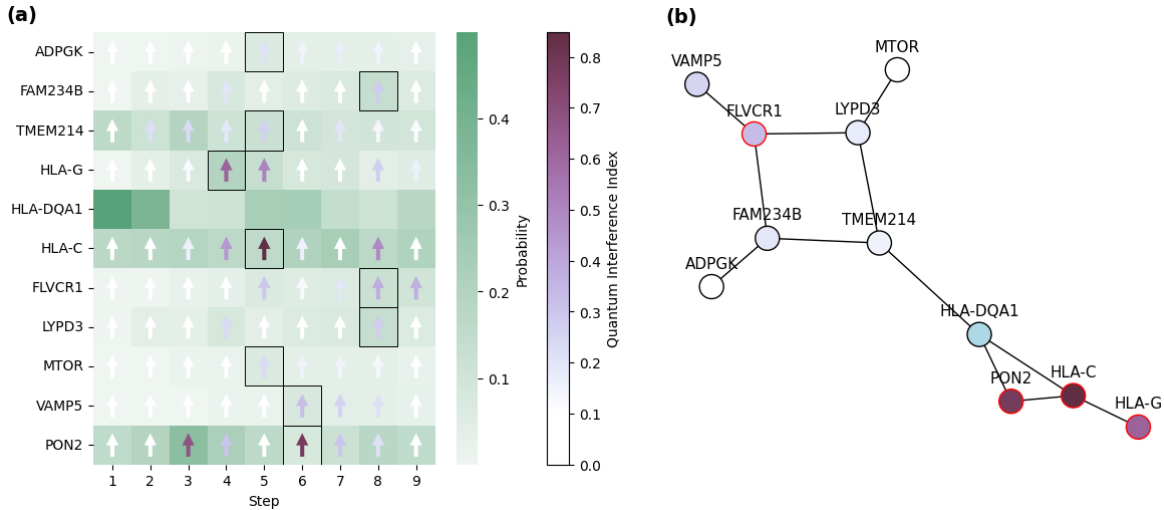


Figure 5. Disease-gene prioritization from experimentally measured quantum-walk dynamics. (a) Heatmap shows postselected transition probabilities in DTQWs on a graph depicted in Fig. 2(a). Arrows indicate how strongly quantum interference modifies the probability at node i relative to the classical random walk, and black squares mark the maximum quantum interference index (score). (b) Corresponding biological network with node colors reflecting their scores and the four highest-score genes highlighted in red.

The DTQWs applied to the asthma case study operates on an 11-nodes subgraph of the PPI network, selected to meet current hardware limitations. While this restricts direct real-world applicability, it serves as a proof of concept for DTQW-based algorithms and illustrates the transition from quantum-inspired algorithms to their actual implementation on quantum hardware. In addition, it demonstrates the advantages of the proposed circuit design.

Scaling analysis

To assess the scalability of the proposed algorithm, we compare its resource requirements with those of the state-of-the-art approach described by Sato and Saito²⁹. Their quantum circuit design for implementing DTQWs on complex networks requires $\lceil \log_2 N \rceil + \lceil \log_2 |E| \rceil$ qubits. However, this approach relies heavily on multi-controlled Toffoli gates in both shift and coin operators, whose transpilation grows exponentially with the number of qubits involved. Eventually, the coin operator circuit exhibits depth scaling as $\text{poly}(N)$, whereas the depth of shift operator scales as $\text{poly}(|E|)$. This leads to rapidly increasing circuit depth even for relatively small graphs. For instance, a 6-qubit implementation of a single DTQW step on an 8-node, 8-edge graph with maximum degree 3 already decomposes into a circuit containing 1,218 entangling layers, based on the best configuration produced by Qiskit's `transpile` function (v1.4.3) at the maximum optimization level without connectivity constraints. When the constraints of heavy-hex qubit connectivity are taken into account, the number of entangling layers increases further, reaching 2,882. The recent paper³⁰ demonstrates that the use of dual-register encoding results in an improved depth scaling, $\text{poly}(N)$, independent of the number of edges (circuit depth $\propto N^{1.9} \times t$ and exceeds 3×10^3 for $N = 10$ and $t = 1$ in the examples considered). Given the limitations of current quantum hardware, deep circuits for $N \geq 9$ (requiring at least $2 \lceil \log_2 N \rceil \geq 8$ qubits) remain challenging for implementation in pre-fault-tolerant quantum computers.

In contrast, in our approach the depth of both the coin and shift operators is independent of N and $|E|$ due to their parallel implementation in qubit space, see Fig. 1. For the same 8-node, 8-edge example graph as in Ref.²⁹, a single DTQW step generated with our framework requires only 11 entangling layers in QPU with all-to-all connectivity and 28 entangling layers under the heavy-hex connectivity, reducing the circuit depth by two orders of magnitude compared to the aforementioned design. This reduction stems from the scaling properties of our method, in which circuit depth grows primarily with the maximum node degree. Specifically, the depth of the coin operator corresponding to a node with the highest degree roughly scales as $2.15 \times 2^{\max_i(k_i)}$ in idealized settings without connectivity constraints, and as $3.75 \times 2^{\max_i(k_i)}$ when heavy-hex connectivity constraints are imposed by hardware. For graphs with a fixed maximum degree, our approach efficiently trades circuit depth for qubit count, reducing the overall circuit volume from $(\lceil \log_2 N \rceil + \lceil \log_2 |E| \rceil) \times (\text{poly}(N) + \text{poly}(|E|)) \times t$ in Ref.²⁹ or $2 \lceil \log_2 N \rceil \times \text{poly}(N) \times t$ in Ref.³⁰ down to $2|E| \times \text{const} \times t$. Since the average number of gate errors is proportional to the circuit volume, the proposed encoding enables larger-scale experiments on current quantum devices.

Table 1 further highlights the scalability of our approach, showing that a 7-step DTQW circuit on a 17-node graph requires fewer than 300 entangling layers. In agreement with the scaling analysis, all three graphs in Table 1, sharing a maximum degree of 3, result in circuits with similar numbers of entangling layers per step despite differences in graph size and structure. Scaling

Table 2. Gene prioritization results.

Gene	Node	Score	Relation to asthma
HLA-C	6	0.85	Associated with allergic asthma ⁴⁰
PON2	1	0.78	Therapeutic potential in asthmatics ⁴⁰
HLA-G	8	0.62	Differentially associated with asthmatic features ⁴¹
FLVCR1	5	0.38	A risk factor childhood-onset asthma ³⁹
VAMP5	2	0.32	No known association
LYPD3	4	0.28	No known association
FAM234B	10	0.28	No known association
TMEM214	9	0.27	No known association
MTOR	3	0.23	No known association
ADPGK	11	0.21	No known association

of the proposed framework for DTQW on complex networks is aligned with the roadmaps of QPU hardware providers^{42–44} targeting both the substantial growth in the number of physical qubits (up to millions) and the reduction in gate and readout errors as more advanced error-correction codes are being developed.

Discussion

In this work, we have presented an implementation strategy for DTQWs on current quantum computers and explored their potential application to gene prioritization in biological networks. The proposed framework has been applied to three model biological graphs, whose corresponding quantum circuits have been successfully executed with reasonable fidelity on current quantum devices at the scale of up to 40 qubits and 287 entangling layers. This feasibility within our method is supported by a combination of the following:

- improved gate performance in available hardware,
- encoding information within a specific (single-excitation) symmetry sector of the qubit space,
- circuit optimization unlocked by the sparsity of the used encoding in qubit space,
- the use of postselection to filter measurement outcomes respecting the symmetry.

Taken together, these features overcome limitations that had previously restricted DTQW experiments to fewer than 10 qubits.

Our results indicate that, with efficient quantum state encoding, the maturity of current quantum computers suffices to solve real-world problems in network medicine, albeit at small scale. The asthma case study illustrates the transition from early quantum-inspired algorithms^{5–8} to fully hardware-realized quantum algorithms. Our QPU-experiment-based node-prioritization method successfully identifies asthma-associated proteins in a reduced PPI graph, with the findings supported by dedicated biological studies. Overall, the results highlight both the practical advantages of the proposed circuit design and the requirements posed by existing hardware.

The actual performance of the proposed DTQW algorithm in practice is limited by the average noise level in gates and measurements, as noise leads to the exponential decay of the fraction of symmetry-respecting bitstrings in postselection. Moreover, multiple bit-flip errors may remain undetectable by postselection if the total number of excitation is preserved. These vulnerabilities should be taken into account in the design of larger-scale experiments. Incorporating advanced noise mitigation strategies could improve the experimental results and allow deeper circuits with more steps. For instance, adapting algorithms like the tensor-network error mitigation^{45,46} for postselection could help reduce error accumulation as circuit depth grows.

As quantum hardware evolves, it will feature more qubits with improved fidelity and connectivity. Although higher fidelity and richer connectivity will enable the reliable execution of longer walk sequences on more complicated graphs, circuit depth will remain a limiting factor. Due to the abundance in physical qubits, whose number is expected to grow up to millions according to the quantum technology roadmaps^{42–44}, it is much more appealing from a technological perspective to trade the circuit depth for the qubit count in order to exploit the full capability of current hardware. It is the encoding used in our approach that extensively exploits this trade-off, allowing to deal with a wider range of graph structures (of larger sizes and

higher densities) as quantum hardware improves. This is a more tractable path forward—compared to boosting fidelities alone—toward practical implementation of complex quantum system dynamics, challenging classical simulations.

While the present study focuses on the scaling behavior of single-particle DTQWs, the underlying framework is inherently extensible to multi-particle, correlated-walker dynamics by incorporating interaction terms within the same hardware-aware circuit design. For example, it paves the way to implementation of the two-particle DTQW algorithm for distinguishing non-isomorphic graphs⁴⁷. Mathematical structure of interacting (entangled) walkers represents an interesting direction for future research, as the dimension of their tensor-product Hilbert space exponentially increases with the number of walkers and becomes computationally expensive in classical simulations. In contrast, quantum-circuit representations can encode such interactions directly through qubit-qubit coupling, offering a clear advantage. This advantage can find application in multi-walker node-prioritization methods applied to heterogeneous biological networks.

Methods

Biological data preparation

We extract gene subgraphs from the Bioplex 3.0 PPI network⁴⁸. Nodes are randomly sampled from the network until the resulting subgraph contains at least one asthma-associated gene, as identified by GWAS summary statistics available through the Open Targets Platform⁴⁹. The asthma-related gene serves as the seed node in the network, at which the initial position of quantum walker is located. We restrict to graphs, whose nodes have degree 3 or lower, and contain 20 or less edges. These restrictions effectively balance the complex graph structure with the capabilities of current QPU hardware.

Efficient quantum-walk circuit construction

DTQW evolution operator for step t reads $U = (CS)^t$ so that each step consists of sequential applications of the shift (S) and coin (C) operators. The ordering of operators is dictated by the initial state (3), which is an invariant state of the Grover coin operator. The latter is defined on a graph with nodes $i = 1, \dots, N$ through

$$C = \bigoplus_{i=1}^N C_i, \quad (5)$$

where $C_i = 2|s_i\rangle\langle s_i| - I_i$,

$$|s_i\rangle = \frac{1}{\sqrt{k_i}} \sum_{j:(i,j) \in E_{\text{dir}}} |i \rightarrow j\rangle, \quad (6)$$

and $k_i = \sum_{j:(i,j) \in E_{\text{dir}}} 1$ is the degree of node i .

To implement the Grover coin operator (5), two strategies can be utilized. First, a proposal by Sato et al.²⁹ effectively maps the uniform superposition $|s_i\rangle$ to the qubit state $|0\dots 0\rangle$ via the inverse of the initial state preparation process and reflects the state about $|0\dots 0\rangle$ (implements the unitary $2|0\dots 0\rangle\langle 0\dots 0| - I$). Then the reflected state is mapped back to the original coin subspace, preserving the structure of the walker's state (1), i.e.,

$$C_i |\psi\rangle = 2\langle s_i | \psi \rangle |s_i\rangle - |\psi\rangle. \quad (7)$$

We find this approach efficient when the nodes have degree $k_i > 3$.

However, for lower node degrees $k_i \leq 3$, we propose and utilize a second approach based on embedding the coin operator C_i (acting in the k_i -dimensional subspace spanned by vectors $\{|i \rightarrow j\rangle\}_{j:(i,j) \in E_{\text{dir}}}$) into the Hilbert space of k_i qubits (with the qubit space dimension being 2^{k_i}),

$$C_i^{\text{qubits}} = I + \sum_{n=1}^{k_i} \sum_{m=1}^{k_i} \left((C_i^{\text{edges}})_{nm} - \delta_{nm} \right) |\text{bin}(2^{n-1})\rangle\langle \text{bin}(2^{m-1})|, \quad (8)$$

where $\text{bin}(x)$ denotes the binary representation of integer x , with $|\text{bin}(2^{n-1})\rangle$ being a single-excitation (bracelet) state (one of $|0\dots 001\rangle, |0\dots 010\rangle, \dots, |1\dots 000\rangle$).

To optimize the decomposition of multi-qubit gates in C_i^{qubits} , we exploit the fact that the Qiskit transpiler can reduce the number of two-qubit operations (and the circuit depth) when the computational basis is rotated⁵⁰. In our case, we permute the bracelet states $|0\dots 001\rangle, |0\dots 010\rangle, \dots, |1\dots 000\rangle$ with the domain-wall (DW) states $|0\dots 001\rangle, |0\dots 011\rangle, \dots, |1\dots 111\rangle$, which is accomplished by the CNOT cascade before and after the unitary operation C_i^{DW} , as illustrated in Fig. 6. C_i^{DW} is

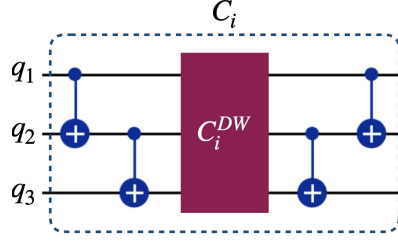


Figure 6. Depth-efficient structure of the coin operator ($k_i = 3$).

given by an analogue of Eq. (8) with the corresponding change in the qubit states. Importantly, the transformation in Fig. 6 temporarily changes the basis in which the Grover coin is expressed, allowing us to significantly reduce the complexity of the decomposed circuit: the number of 2-qubit native entangling gates and the transpiled-circuit depth is approximately halved as compared to those in transpilation of Eq. (8) at the first place. Therefore, the implemented basis rotation reduces entangling operations without altering the logical structure of the algorithm and is particularly useful in pre-fault-tolerant experiments.

Implementation of the shift operator (4) reduces to individual partial swap gates acting on pairs of qubits, see α -gates in Fig. 1(c). The resulting decomposition follows the same sequence of CNOT gates used to realize a full swap, but is augmented with the single-qubit rotation gates, leading to a partial rather than complete swap.

Executing quantum walks on current quantum computers becomes challenging on superconducting hardware with heavy-hex connectivity, as this topology imposes strong constraints on qubit mapping. The decomposition of shift operators into hardware-native gates is particularly sensitive to these topological limitations, since a shift operation between non-adjacent qubits must be transpiled into a sequence of CNOT gates, thereby increasing circuit depth. To mitigate this effect, we transpile each DTQW circuit using Qiskit `transpile` function 100 times and select the final configuration in the following way. First, we restrict to layouts where the qubits involved in α -gates are physically separated by no more than eight edges on the connectivity map. Second, we exclude layouts with ancilla qubits. Third, we avoid qubits with high readout error in the layout to maximize the fraction of bitstrings retained in the postselection process. Altogether, these criteria ensure that the selected layouts reduce noise accumulation in the two-qubit gates and support a reasonable level of accuracy in circuits that may include more than 200 entangling layers and measurements on up to 40 qubits.

Experimental setup

We have performed the experiments on superconducting devices with fixed-frequency transmon qubits as data qubits connected via tunable couplers: the 24- and 40-qubit experiments on IBM Heron R2 QPU `ibm_kingston` and the 36-qubit experiment on IBM Heron R3 QPU `ibm_pittsburgh`. These devices have 156 qubits, with the median single-qubit gate errors, two-qubit gate errors, and readout errors being 2.1×10^{-4} , 1.7×10^{-3} , and 4.1×10^{-3} , respectively, for `ibm_pittsburgh` and 2.2×10^{-4} , 2.1×10^{-3} , and 8.4×10^{-3} , respectively, for `ibm_kingston` according to the latest calibration prior the experiment. The execution of quantum circuits is performed remotely via IBM Quantum’s cloud infrastructure in Qiskit v1.4.3, an open-source, Python-based, high-performance software stack for quantum computing^{51,52}.

We set the number of measurement shots to progressively increase with each DTQW step t so as to ensure statistical relevance of the data affected by noise. The number of measurement shots is $5.3 \times 10^5 \times 1.1^t$ ($5.3 \times 10^5 \times 1.6^t$) in the case of the 24-qubit (36- and 40-qubit) experiment, which remains below 10^7 for the steps implemented.

QPU data processing

The information about the walker location on graph edges $(i, j) \in E_{\text{dir}}$ is encoded into the excitation position $q_{(i,j)}$ inside a bitstring b of length $2|E|$, with $b_q = \delta_{q, q_{(i,j)}}$. Due to the presence of noise in raw output bitstrings of QPU, the number of excitations is not exactly equal to unity, with no essential tool being available to distinguish the noisy excitation from the true excitation at the level of individual bitstrings. The noise-contaminated probability to observe the walker in edge $(i, j) \in E_{\text{dir}}$ is therefore given by

$$P_{(i,j)}^{\text{raw}} = \frac{\sum_b \delta_{b_{q_{(i,j)}}, 1}}{\sum_{b,q} \delta_{b_q, 1}}. \quad (9)$$

The probability of a walker to be on node i is a marginal probability $P_i^{\text{raw}} = \sum_{j:(i,j) \in E_{\text{dir}}} P_{(i,j)}^{\text{raw}}$.

The effect of postselection is to restrict the bitstrings b in Eq. (9) to a single-excitation subspace, the Hamming weight

$|b| = 1$. This leads to the probability

$$P_{(i,j)}^{\text{ps}} = \frac{\sum_{b:|b|=1} \delta_{b_{q(i,j)},1}}{\sum_{b:|b|=1} 1}. \quad (10)$$

The probability of a walker to be on node i is a marginal probability $P_i^{\text{ps}} = \sum_{j:(i,j) \in E_{\text{dir}}} P_{(i,j)}^{\text{ps}}$. The fraction of bitstrings retained in the postselection procedure equals $(\sum_{b:|b|=1} 1)/(\sum_b 1)$ and typically decays exponentially with the circuit depth and number of qubits, with the decay rate depending on the gate and measurement error rate of QPU. To make allowance for the decay, we sequentially increase the number of measurement shots with the DTQW step t as reported in Experimental Setup.

Performance metrics

We verify the correctness of the implemented DTQWs by comparing with the classical simulation. To compare the ideal probability distribution Q with the experimental one, P , we exploit the Hellinger fidelity $F_{\text{H}}(P, Q) = (1 - h^2(P, Q))^2 = (\sum_i \sqrt{P_i Q_i})^2$, where the Hellinger distance $h(P, Q)$ between P and Q is defined through $h^2(P, Q) = \frac{1}{2} \sum_i (\sqrt{P_i} - \sqrt{Q_i})^2$. The Hellinger fidelity $F_{\text{H}}(P, Q)$ satisfies the property $0 \leq F_{\text{H}}(P, Q) \leq 1$ and is exactly equal to unity if and only if the two distributions are identical.

In a long-time DTQWs over complex network ($t \gg 1$), the theoretical distribution Q fluctuates around the uniform distribution of the walker over the edge states $|i \rightarrow j\rangle$, $(i, j) \in E_{\text{dir}}$. The baseline distribution of the walker over the nodes i_1, i_2, \dots is therefore $R = (k_{i_1}, k_{i_2}, \dots) / \sum_j k_j$, where k_i is the degree of node i , also known as a stationary or steady-state distribution in the theory of classical random walks on graphs⁵³. In the experiment, the observed distribution P tends to R even faster than the theoretical distribution Q due to the accumulating effect of noise. Hence, the effect of noise on the Hellinger fidelity $F_{\text{H}}(P, Q)$ is masked, when both P and Q are close to R . In order to make correction for the steady-state baseline distribution R , we consider the baseline-corrected Hellinger fidelity

$$F_{\text{HBC}}(P, Q|R) = \frac{F_{\text{H}}(P, Q) - F_{\text{H}}(R, Q)}{1 - F_{\text{H}}(R, Q)}. \quad (11)$$

By construction, $F_{\text{HBC}}(P, Q|R) \leq 1$ and equals unity if and only if $F_{\text{H}}(P, Q) = 1$. If the baseline fidelity $F_{\text{HBC}} \leq 0$, then the theoretical distribution Q is in better agreement with the baseline distribution R (null hypothesis) than the experimental distribution P .

Node prioritization method

Propagation of a quantum walker through a network is governed by quantum superposition and interference of amplitude states. Unlike classical diffusion processes, the DTQWs does not converge to a stationary distribution; instead, transition probabilities oscillate over time. During these oscillations some nodes i exhibit positive (negative) surges in probability $P_i^{\text{q}}(t)$ as compared to the probability $P_i^{\text{cl}}(t)$ in classical random walk. The latter is defined through $P_j^{\text{cl}}(t+1) = \sum_i M_{ij} P_i^{\text{cl}}(t)$, where M is a stochastic matrix defining the Markov chain, $M_{ij} = \alpha \delta_{ij} + (1 - \alpha) \delta_{(i,j) \in E_{\text{dir}}} k_i^{-1}$. We use the interference quantifier $|P_i^{\text{q}}(t) - P_i^{\text{cl}}(t)|$ to highlight the nodes with constructive (destructive) quantum interference, thus indicating their functional importance within the network. We exploit the phenomenon of quantum interference to identify the key nodes (i.e., target genes) in biological networks. To quantify this effect, we introduce a quantum interference index (QII)

$$I_i(t) = \frac{|P_i^{\text{q}}(t) - P_i^{\text{cl}}(t)|}{\sum_j [P_j^{\text{q}}(t)]^2}. \quad (12)$$

The collision probability $\sum_j [P_j^{\text{q}}(t)]^2 \equiv \langle P^{\text{q}} \rangle$ makes allowance for the average probability of the walker, since the wider is the distribution of the walker, the less is the base for the quantum interference. Importantly, QII vanishes not only for step $t = 0$ (initialization of the walker on a seed node) but also for $t = 1$ because the initial spreading involves no interference.

A prioritization score is defined as the maximum QII over time,

$$S_i = \max_t I_i(t). \quad (13)$$

Since the experimental distribution $P_i^{\text{q}}(t)$ approaches to the steady-state baseline distribution $R = (k_{i_1}, k_{i_2}, \dots) / \sum_j k_j$ due to noise and $R = \lim_{t \rightarrow \infty} P_i^{\text{cl}}(t)$ ⁵³, QII vanishes in long-time realistic (noisy) quantum computation. The maximum QII in Eq. (13) is attained within a timescale of QPU qubits' coherence.

We associate target genes with the nodes that have the highest scores (exhibit the strongest interference during the DTQWs). This method reveals structural relationships that go beyond simple connectivity and highlights nodes that may be distant

from the seed but are nonetheless significant, offering a fundamentally different perspective on biological networks. The method captures both spatial and temporal aspects of DTQW dynamics, effectively marking the distinctive nodes in walker's propagation through the network.

Data availability

Data is available from the corresponding author upon reasonable request.

Code availability

The codes used to generate data for this paper are available from the corresponding author upon reasonable request.

References

1. Bose, A., Rhrissorakrai, K., Utro, F., Parida, L. & the Quantum for Healthcare Life Sciences Consortium. Advancing single-cell omics and cell-based therapeutics with quantum computing. *Nature Reviews Molecular Cell Biology*, <https://doi.org/10.1038/s41580-025-00918-0> (2026).
2. Kempe, J. Quantum random walks: An introductory overview. *Contemporary Physics* **44**, 307–327 (2003).
3. Venegas-Andraca, S. E. Quantum walks: a comprehensive review. *Quantum Information Processing* **11**, 1015–1106 (2012).
4. Maniscalco, S. *et al.* Quantum network medicine: rethinking medicine with network science and quantum algorithms. arXiv:2206.12405 (2022).
5. Goldsmith, M. *et al.* Link prediction with continuous-time classical and quantum walks. *Entropy* **25**, 730 (2023).
6. Saarinen, H., Goldsmith, M., Wang, R.-S., Loscalzo, J. & Maniscalco, S. Disease gene prioritization with quantum walks. *Bioinformatics* **40**, btae513 (2024).
7. Dubovitskii, V., Bose, A., Utro, F. & Parida, L. On quantum random walks in biomolecular networks. arXiv:2506.06514 (2025).
8. Park, J. *et al.* Advancing understanding of long covid pathophysiology through quantum walk-based network analysis. arXiv:2501.15208 (2025).
9. Córcoles, A. D. *et al.* Challenges and opportunities of near-term quantum computing systems. *Proceedings of the IEEE* **108**, 1338–1352 (2020).
10. Fauseweh, B. Quantum many-body simulations on digital quantum computers: State-of-the-art and future challenges. *Nature Communications* **15**, 2123 (2024).
11. Cai, Z. *et al.* Quantum error mitigation. *Rev. Mod. Phys.* **95**, 045005 (2023).
12. Filippov, S. N., Maniscalco, S. & García-Pérez, G. Scalability of quantum error mitigation techniques: from utility to advantage. arXiv:2403.13542 (2024).
13. Eisert, J. & Preskill, J. Mind the gaps: The fraught road to quantum advantage. arXiv: 2510.19928 (2025).
14. Zimborás, Z. *et al.* Myths around quantum computation before full fault tolerance: What no-go theorems rule out and what they don't. arXiv: 2501.05694 (2025).
15. Acasiete, F., Agostini, F. P., Moqadam, J. K. & Portugal, R. Implementation of quantum walks on IBM quantum computers. *Quantum Inf. Process.* **19**, 426 (2020).
16. Koch, D., Samodurov, M., Projansky, A. & Alsing, P. M. Gate-based circuit designs for quantum adder inspired quantum random walks on superconducting qubits. arXiv: 2012.10268 (2020).
17. Shakeel, A. Efficient and scalable quantum walk algorithms via the quantum Fourier transform. *Quantum Inf. Process.* **19**, 323 (2020).
18. Georgopoulos, K., Emary, C. & Zuliani, P. Comparison of quantum-walk implementations on noisy intermediate-scale quantum computers. *Phys. Rev. A* **103**, 022408 (2021).
19. Razzoli, L., Cenedese, G., Bondani, M. & Benenti, G. Efficient implementation of discrete-time quantum walks on quantum computers. *Entropy* **26**, 313 (2024).
20. Wing-Bocanegra, A. & Venegas-Andraca, S. E. Circuit implementation of discrete-time quantum walks via the shunt decomposition method. *Quantum Inf. Process.* **22**, 146 (2023).

21. Wadhia, V., Chancellor, N. & Kendon, V. Cycle discrete-time quantum walks on a noisy quantum computer. *Eur. Phys. J. D* **78**, 29 (2024).
22. Singh, S. *et al.* Quantum circuits for the realization of equivalent forms of one-dimensional discrete-time quantum walks on near-term quantum hardware. *Phys. Rev. A* **104**, 062401 (2021).
23. Nandi, B., Singha, S., Datta, A., Saha, A. & Chakrabarti, A. Robust implementation of discrete-time quantum walks in any finite-dimensional quantum system. *Modern Physics Letters A* **40**, 2550035 (2025).
24. Saha, A., Majumdar, R., Saha, D., Chakrabarti, A. & Sur-Kolay, S. Asymptotically improved circuit for a d -ary grover's algorithm with advanced decomposition of the n -qudit Toffoli gate. *Phys. Rev. A* **105**, 062453 (2022).
25. Zhou, Y., Stoudenmire, E. M. & Waintal, X. What limits the simulation of quantum computers? *Phys. Rev. X* **10**, 041038 (2020).
26. Nzongani, U. & Arnault, P. Adjustable-depth quantum circuit for position-dependent coin operators of discrete-time quantum walks. *Quantum Inf. Process.* **23**, 193 (2024).
27. Mukai, K. & Hatano, N. Discrete-time quantum walk on complex networks for community detection. *Phys. Rev. Res.* **2**, 023378 (2020).
28. Singh, A. & Sachan, B. A quantum approach to walk on networks. In *2021 6th International Conference on Signal Processing, Computing and Control (ISPCC)*, 636–643 (2021).
29. Sato, R. & Saito, K. Circuit implementation of discrete-time quantum walks on complex networks. In *2024 IEEE International Conference on Quantum Computing and Engineering (QCE)*, vol. 2, 376–377 (IEEE, 2024).
30. Sato, R. Coined quantum walks on complex networks for quantum computers. arXiv:2512.16400 (2025).
31. Wing-Bocanegra, A., Quintero-Narvaez, C. E. & Venegas-Andraca, S. E. Circuit implementation and analysis of a quantum-walk based search complement algorithm. *Scientific Reports* **15**, 4865 (2025).
32. Geller, M. R. *et al.* Universal quantum simulation with prethreshold superconducting qubits: Single-excitation subspace method. *Physical Review A* **91**, 062309 (2015).
33. Cabello, A. Bell's theorem with and without inequalities for the three-qubit Greenberger-Horne-Zeilinger andwstates. *Phys. Rev. A* **65**, 032108 (2002).
34. Prabhu, P. & Brun, T. A. Influence of coin symmetry on infinite hitting times in quantum walks. *Phys. Rev. A* **105**, 032206 (2022).
35. Agrawal, M., Zitnik, M. & Leskovec, J. Large-scale analysis of disease pathways in the human interactome. In *Pacific Symposium on Biocomputing*, vol. 23, 111–122 (2018).
36. Menche, J. *et al.* Uncovering disease-disease relationships through the incomplete interactome. *Science* **347**, 1257601 (2015).
37. Clay, S. M. *et al.* Fine-mapping studies distinguish genetic risks for childhood- and adult-onset asthma in the HLA region. *Genome Med.* **14**, 55 (2022).
38. Cerezo, M. *et al.* The NHGRI-EBI GWAS Catalog: standards for reusability, sustainability and diversity. *Nucleic Acids Research* **53**, D998–D1005 (2024).
39. Ferreira, M. A. R. *et al.* Genetic architectures of childhood- and adult-onset asthma are partly distinct. *Am. J. Hum. Genet.* **104**, 665–684 (2019).
40. Winnica, D. E. *et al.* Airway epithelial paraoxonase-2 in obese asthma. *PLoS One* **17**, e0261504 (2022).
41. Ribeyre, C. *et al.* HLA-G haplotypes are differentially associated with asthmatic features. *Front. Immunol.* **9**, 278 (2018).
42. Hardware for useful quantum computing. <https://www.ibm.com/quantum/hardware#roadmap>. Accessed: 2026-02-19.
43. Quantum computing roadmap. <https://quantumai.google/roadmap>. Accessed: 2026-02-19.
44. Development Roadmap. <https://meetiqm.com/technology/roadmap/>. Accessed: 2026-02-19.
45. Filippov, S., Leahy, M., Rossi, M. A. C. & García-Pérez, G. Scalable tensor-network error mitigation for near-term quantum computing. arXiv: 2307.11740 (2023).
46. Fischer, L. E. *et al.* Dynamical simulations of many-body quantum chaos on a quantum computer. *Nat. Phys.* **22**, 302–307 (2026).

47. Berry, S. D. & Wang, J. B. Two-particle quantum walks: Entanglement and graph isomorphism testing. *Physical Review A* **83**, 042317 (2011).
48. Huttlin, E. L. *et al.* Dual proteome-scale networks reveal cell-specific remodeling of the human interactome. *Cell* **184**, 3022–3040.e28 (2021).
49. Buniello, A. *et al.* Open targets platform: facilitating therapeutic hypotheses building in drug discovery. *Nucleic Acids Research* **53**, D1467–D1475 (2024).
50. Synthesize unitary operations, IBM quantum documentation. <https://quantum.cloud.ibm.com/docs/en/guides/synthesize-unitary-operators> (2025).
51. IBM Quantum Cloud Compute Resources. <https://quantum.cloud.ibm.com/computers>. Accessed: 2026-02-19.
52. Javadi-Abhari, A. *et al.* Quantum computing with Qiskit. arXiv:2405.08810 (2024).
53. Lovász, L. Random walks on graphs: A survey. *Combinatorics, Paul Erdos is Eighty* **2**, 1–46 (1993).

Acknowledgements

This work was conducted within the framework of the Health Care and Life Sciences Quantum Working Group. The authors would like to thank Guillermo García-Pérez for useful conversations regarding this work.

Author contributions

V.D., S.F., F.U., A.B., and L.P. conceptualized the study; S.F. conceived the experiment; A.B. performed data preprocessing; S.F., V.D., and F.U. performed the experiments; V.D. processed the results and drafted the original version of the manuscript; V.D., F.U., A.B., and S.F. interpreted the results and wrote the manuscript; L.P. and S.M. supervised the work; all authors participated in the discussion of the results.

Ethics declarations

Competing interests: The authors declare no competing interests.